

Quasi-periodic flat-band model constructed by molecular-orbital representation

Tomonari Mizoguchi and Yasuhiro Hatsugai

*Department of Physics, University of Tsukuba, Tsukuba, Ibaraki 305-8571, Japan**

(Dated: June 11, 2025)

We construct a tight-binding model that hosts both a quasi-periodic nature and macroscopically-degenerate zero-energy modes. The model can be regarded as a counterpart of the Aubry-André-Harper (AAH) model, which is a paradigmatic example of the quasi-periodic tight-binding model. Our main focus is on the many-body state where the flat-band-like degenerate zero-energy modes are fully occupied. We find a characteristic sublattice dependence of the particle density distribution. Further, by analyzing the hyperuniformity of the particle density distribution, we find that it belongs to the class-I hyperuniform distribution, regardless of the model parameter. We also show that, upon changing the parameter, the finite-energy modes exhibit the same extended-to-localized transition as that for the original AAH model.

I. INTRODUCTION

Interference effects in single-particle physics cause characteristic localization [1]. In translationally invariant systems where the momentum-space representation is applicable, the localization is manifested by existence of characteristic band structure called flat bands [2, 3], i.e., the completely dispersionless band in the entire momentum space. In flat bands, macroscopic number of single-particle states degenerate. Hence, the linear combinations among extended Bloch wave functions with the same energy lead to the spatially-localized eigenstates. In many cases, one can construct the localized eigenstates that has a compact support in the real space, which are called the compact localized states (CLSs) [4–8].

Recently, the physics of flat bands has been explored in systems with broken translational symmetry. Breaking translational symmetry typically lifts the degeneracy of flat bands since flat bands arise from subtle interference effects. Hence, in many previous works, the spatial inhomogeneity is introduced as a perturbation against the flat band model in order to investigate how the flat band states behave toward them. Various types of spatial inhomogeneities have been considered, such as randomness [9–18], linear potentials [19], magnetic flux [20], and quasi-periodicity [21, 22].

Meanwhile, several atypical cases have also been studied, that is, the flat-band-like degenerate states survive even in the presence of spatial inhomogeneity. In the previous studies, the authors have proposed a systematic construction method of the tight-binding models that contain randomness but the macroscopically-degenerate states reminiscent of flat bands remain [23–25]. We refer to our model construction scheme the molecular-orbital (MO) representation, since we write down the Hamiltonian with taking the “molecules” [i.e., the states composed of the linear combination of a finite number of atomic orbitals (AOs)] as basic units. This construction guarantees the existence of the degenerate zero-energy modes when the number of MOs is smaller than that of the AOs [8, 25–30].

In the present work, we explore the intersection between the

quasi-periodicity and the flat bands. Specifically, we propose a model that can be regarded as a counterpart of the Aubry-André-Harper (AAH) model [31, 32]. The AAH model, which is the one-dimensional chain with the incommensurate on-site potential, is a prime example of quasi-periodic tight-binding models. Our Hamiltonian is, on the other hand, defined on a saw-tooth lattice [Fig. 1(a)], which has two sublattice degrees of freedom per unit cell. We apply the MO representation to this system, taking triangular molecules as units. To relate the model with the AAH model, we put the quasi-periodicity in the coefficients appearing in the MOs. Remarkably, as far as the finite-energy sector is concerned, the resulting tight-binding model has common eigenenergies as the AAH model up to the constant shift, and the eigenstates are also related to those of the AAH model. Hence, the finite-energy modes exhibit the same extended-to-localized transition as that for the original AAH model.

Our main focus is, however, not on the finite-energy modes but on the many-body ground state for the half-filled systems of fermions, where the degenerate zero-energy modes are fully occupied. We investigate the spatial distribution of the particle density of that state. We first address the characteristic sublattice dependences of the particle density distribution. Then, we perform the hyperuniformity analysis on the particle density distribution. The notion of the hyperuniformity [33–36] has been introduced to characterize the point distribution in the continuum space having suppressed particle density fluctuation in long wave length. Recently, the hyperuniformity has been employed to characterize the particle density distributions and spin configurations of the lattice models [37–42]. Inspired by these developments, we apply this scheme to our system. As a result, we find that the particle density distribution belongs to the class-I hyperuniformity, regardless of the parameter that characterizes the strength of the quasi-periodic part.

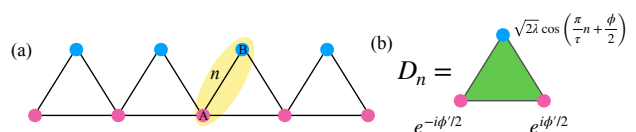


FIG. 1. Schematic figures of (a) a saw-tooth lattice and (b) the MO of Eq. (1).

* mizoguchi@rhodia.ph.tsukuba.ac.jp

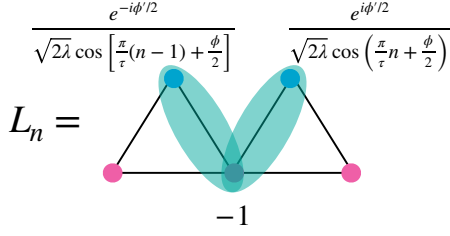


FIG. 2. Schematic figure of the compact localized state of Eq. (8).

The rest of this paper is organized as follows. In Sec. II, we introduce our tight-binding model. In Sec. III, we present the main results of this paper, namely, the characteristic real-space particle density distribution for the many-body state with the zero modes being fully occupied. In particular, we analyze them in terms of the hyperuniformity. In Sec. IV, we address the properties of the finite-energy modes, paying attention to their transition from the extended to the localized states. Finally, we present the summary of this paper in Sec. V.

II. MODEL

We consider the tight-binding Hamiltonian defined on a saw-tooth lattice [Fig. 1(a)]. In a saw-tooth lattice, each unit cell contains two sublattices, A and B. We consider the system composed of L unit cells and impose the periodic boundary condition. For future use, we denote the number of sites $N_{\text{site}} = 2L$. We write the annihilation operator for a spinless fermion for A (B) sublattice at the unit cell n as $d_{n,A}$ ($d_{n,B}$). We call these operators AOs. Our idea of constructing the quasi-periodic flat-band model is to introduce the MO whose annihilation operator, D_n , is given as

$$D_n = e^{-i\phi'/2} d_{n,A} + \sqrt{2\lambda} \cos\left(\frac{\pi}{\tau}n + \frac{\phi}{2}\right) d_{n,B} + e^{i\phi'/2} d_{n+1,A}, \quad (1)$$

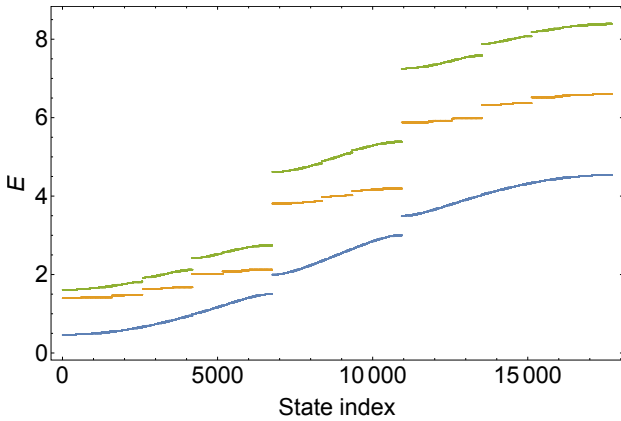


FIG. 3. Energy spectrum of the finite-energy modes of \mathcal{H} , (the degenerate zero-energy modes are eliminated). Blue, orange, and green dots are for $\lambda = 0.5, 2$, and 3 , respectively.

and consider the Hamiltonian

$$H = \sum_n D_n^\dagger D_n. \quad (2)$$

The operator D_n is defined on a triangular unit [see Fig. 1(b)]. λ, τ, ϕ , and ϕ' are the model parameters, with $\lambda \geq 0$. It should be noted that a set of D operators are not orthonormalized basis of the entire system. It is also worth noting that the Hamiltonian is finite-ranged, namely, it contains only the on-site potential and the NN hoppings when being written down in the AO basis.

To clarify the property of this Hamiltonian, we rewrite Eq. (2) in the matrix representation. We align the MOs in the L -component column vector:

$$\mathbf{D} = (D_1, \dots, D_L)^T, \quad (3)$$

and the AOs in the $2L$ -component column vector:

$$\mathbf{d} = (d_{1,A}, d_{1,B}, \dots, d_{L,A}, d_{L,B})^T. \quad (4)$$

For clarity, we use the index n for specifying the component of the \mathbf{D} , while we use the index i for specifying the component of the \mathbf{d} . Then we define the $L \times 2L$ matrix Ψ^\dagger satisfying

$$\mathbf{D} = \Psi^\dagger \mathbf{d}. \quad (5)$$

The explicit form of the matrix elements is

$$[\Psi^\dagger]_{n,i} = \begin{cases} e^{-i\phi'/2}, & i = 2n - 1 \\ e^{i\phi'/2}, & i = 2n + 1 \\ \sqrt{2\lambda} \cos\left(\frac{\pi}{\tau}n + \frac{\phi}{2}\right), & i = 2n \\ 0, & \text{otherwise} \end{cases}. \quad (6)$$

Using this matrix and its Hermitian conjugate, we can write down the Hamiltonian with the AO basis:

$$H = \mathbf{d}^\dagger \mathcal{H} \mathbf{d}, \quad \mathcal{H} = \Psi \Psi^\dagger. \quad (7)$$

Equation (7) indicates that the Hamiltonian matrix \mathcal{H} is positive semidefinite, and that there are at least L zero-energy modes of \mathcal{H} that correspond to the kernel of Ψ^\dagger [25–29, 43]. These degenerate zero-energy modes serve as flat-band-like states, although the translational invariance is absent.

In fact, the zero-energy eigenstates can be given as a set of CLSs. Figure 2 shows the schematic figure of the CLS, L_n . It has a V-shape, and its explicit form is given as

$$L_n = -d_{n,A} + \frac{e^{\phi'/2}}{\sqrt{2\lambda} \cos\left(\frac{\pi}{\tau}n + \frac{\phi}{2}\right)} d_{n,B} + \frac{e^{-\phi'/2}}{\sqrt{2\lambda} \cos\left[\frac{\pi}{\tau}(n-1) + \frac{\phi}{2}\right]} d_{n-1,B}. \quad (8)$$

We find that $\{D_n, L_{n'}^\dagger\} = 0$ holds for any n, n' . Hence, we have $[H, L_n^\dagger] = 0$, meaning that L_n^\dagger serves as a creation operator of the zero-energy eigenmode of H (up to the normalization). Note that L_n 's are not orthogonal to each other, although they are linearly independent.

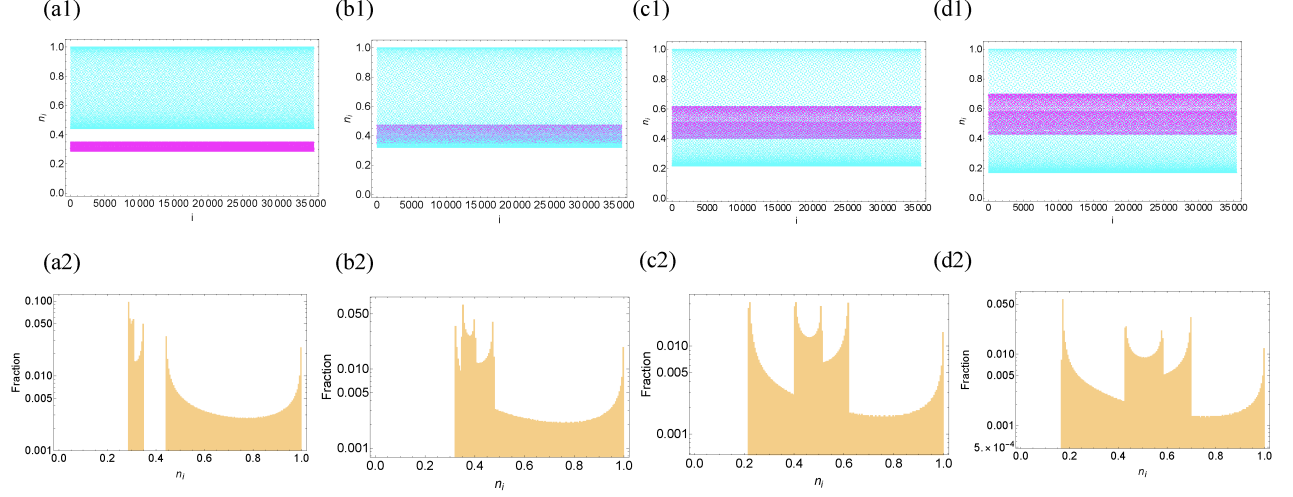


FIG. 4. The real space particle density distribution (the upper row) and its histogram (the lower row). The parameters are (a) $\lambda = 0.5$, (b) $\lambda = 1$, (c) $\lambda = 2$, and (d) $\lambda = 3$. For the upper row, magenta (cyan) points correspond to the sublattice A (B).

Furthermore, the non-zero eigenenergies and eigenstates can be captured by considering the counterpart of \mathcal{H} , which is given as

$$\mathcal{O} = \Psi^\dagger \Psi, \quad (9)$$

$$[\mathcal{O}]_{n,n'} = \begin{cases} e^{-i\phi'}, & n' = n - 1 \\ e^{i\phi'}, & n' = n + 1 \\ 2 + \lambda [1 + \cos(\frac{2\pi}{\tau}n + \phi)], & n' = n \\ 0, & \text{otherwise} \end{cases} \quad (10)$$

Equation (10) indicates that \mathcal{O} corresponds to the Hamiltonian matrix of the AAH model with an additional constant energy shift $2 + \lambda$. The relation between the non-zero energy modes of \mathcal{H} and those of \mathcal{O} is as follows. Let φ_ℓ be a normalized eigenvector of \mathcal{O} that satisfies $\mathcal{O}\varphi_\ell = \varepsilon_\ell\varphi_\ell$ ($\varepsilon_\ell > 0$). Then, it can be shown that $\psi_\ell = \frac{\Psi\varphi_\ell}{\sqrt{\varepsilon_\ell}}$ is a normalized eigenvector of \mathcal{H} [25, 26, 30], since $\mathcal{H}\psi_\ell = \frac{\Psi\Psi^\dagger\Psi\varphi_\ell}{\sqrt{\varepsilon_\ell}} = \frac{\Psi(\mathcal{O}\varphi_\ell)}{\sqrt{\varepsilon_\ell}} = \varepsilon_\ell\psi_\ell$ and $|\psi_\ell|^2 = \frac{\varphi_\ell^\dagger\Psi^\dagger\Psi\varphi_\ell}{\varepsilon_\ell} = \frac{\varphi_\ell^\dagger(\mathcal{O}\varphi_\ell)}{\varepsilon_\ell} = 1$.

In the AAH model, the quasi-periodic nature is introduced via the parameter τ . To be specific, we consider the case where τ is the golden mean, $\tau = (1 + \sqrt{5})/2$. In the numerical calculation, we consider the finite-size system under the periodic boundary condition, hence we replace τ with the rational number τ' that is close to the golden mean, and set the system size L such that it is commensurate with τ' [38]. Such rational numbers can be obtained by the ratio between two neighboring Fibonacci numbers, $\tau' = F_{m+1}/F_m$, where F_m is the m th Fibonacci number [44]. In order that the matrix element of Ψ^\dagger in Eq. (6) has a period L , L has to satisfy $\frac{L}{\tau'} = \frac{LF_m}{F_{m+1}} \in 2\mathbb{Z}$. Hence, we have to choose L and m such that $L = pF_{m+1}$ ($p \in \mathbb{N}$) and $F_m \in 2\mathbb{Z}$. In the following numerical calculation, we consider the case of $m = 21$ ($F_{21} = 10946$) and $p = 1$ (i.e., $L = pF_{22} = 17711$). Also, we set $\phi = \phi' = 0$ for simplicity.

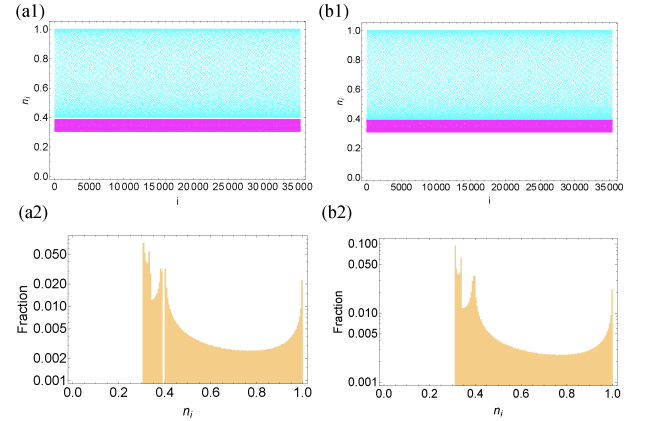


FIG. 5. The real space particle density distribution (the upper row) and its histogram (the lower row). The parameters are (a) $\lambda = 0.625$, (b) $\lambda = 0.645$. For the upper row, magenta (cyan) points correspond to the sublattice A (B).

In Fig. 3, we plot the non-zero energy eigenvalues of \mathcal{H} for three values of λ . We again emphasize that the non-zero energy eigenvalues are identical to those of the conventional AAH model up to the constant energy shift. We also find that there exists a finite-energy gap between the lowest finite-energy mode and the degenerate zero modes, meaning that the degeneracy of the zero modes is L .

III. PARTICLE DENSITY DISTRIBUTION FOR THE FULLY-OCCUPIED ZERO-ENERGY STATES

In this section, we show our main results, namely, the particle density distribution for the fully-occupied zero-energy states.

Let $|\Xi_0\rangle$ be the L -particle state with the zero-energy modes

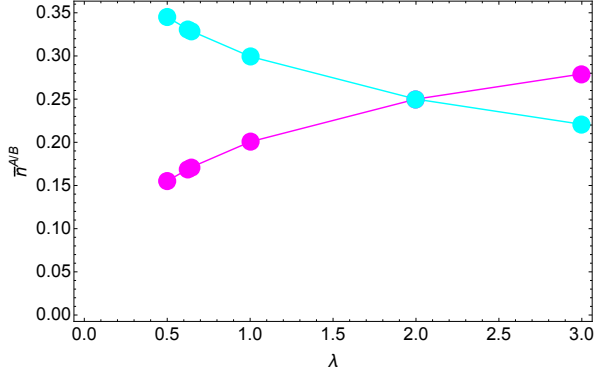


FIG. 6. Sublattice-resolved filling fraction as a function of λ . Magenta and cyan points represent the A and B sublattices, respectively.

of H being fully occupied:

$$|\Xi_0\rangle = \prod_{\ell=1}^L \gamma_{\ell}^{\dagger} |0\rangle, \quad (11)$$

where γ_{ℓ}^{\dagger} ($\ell = 1, \dots, L$) are the creation operators of the orthonormalized zero modes. Note that $|\Xi_0\rangle$ is the ground state of the present model at the half-filling. In fact, in the previous studies, we find that the particle density at the site i can be obtained without explicitly calculating the zero-mode wave functions; rather, it can be calculated by using the matrices Ψ , Ψ^{\dagger} and \mathcal{O} [23, 43] as

$$n_i := \langle \Xi_0 | d_i^{\dagger} d_i | \Xi_0 \rangle = 1 - [\Psi \mathcal{O}^{-1} \Psi^{\dagger}]_{i,i}. \quad (12)$$

Using this formula, we numerically calculate the particle density distribution, which we shall argue below.

A. Real-space profile and its sublattice dependence

In the upper row of Fig. 4, we plot n_i as a function of i for several values of λ . In the lower row of Fig. 4, we plot its histogram. We see that the particle density distribution of the A sublattice has a smaller fluctuation in terms of the positional dependence than that of the B sublattice. This overall tendency does not depend on λ . Quantitatively, the width of the histogram becomes broader as λ becomes larger. In more detail, in the histogram, the contributions from the A sublattice and the B sublattice are separated for $\lambda \lesssim 0.645$, and they overlap for $\lambda \gtrsim 0.645$, as we show in Fig. 5.

Figure 6 shows the λ dependence the sublattice-resolved filling fraction,

$$\bar{n}^{A/B} = \frac{1}{N_{\text{site}}} \sum_{i \in A/B} n_i. \quad (13)$$

We see that $\bar{n}^A < \bar{n}^B$ for $\lambda < 2$ and $\bar{n}^A > \bar{n}^B$ for $\lambda > 2$. Interestingly, the sublattice-resolved average particle density balances at $\lambda = 2$, which is the critical point of the extended to the localized transition for the original AAH model. This indicates that $\lambda = 2$ can be regarded as a “hidden symmetric

point”, although the real-space particle density distribution does not change qualitatively. In fact, we can prove this balance of the particle density by using the special feature of the duality point of the original AAH model, that is, the kinetic energy and the potential energy are the same for all the eigenstates for $\lambda = 2$. See Appendix A for details.

B. Hyperuniformity analysis

To further shed light on the characteristic features of the particle density distribution, we analyze it in terms of hyperuniformity. In the literature, the hyperuniformity has mainly been used to characterize the point-particle density distribution in the continuous space \mathbb{R}^d [33–36, 45, 46]. Here, we use a different definition from those used in the previous works. To be specific, we replace the integral over the continuous space in the original definitions with the summation over the lattice points, since lattices on which our charge distribution is defined preserve discrete translational invariance. By adopting this definition, we exploit the fluctuations of the charge distribution itself rather than the spatial distribution of the lattice on which it is defined.

The explicit definitions of the quantities to evaluate the hyperuniformity are as follows. Let $N_{i_c}(R)$ be the total charge contained in the line of length $2R$ centered at the site i_c , as

$$N_{i_c}(R) = \sum_{i: |i-i_c| \leq R} n_i. \quad (14)$$

Note that the site label i is defined in accordance with the element of \mathbf{d} in Eq. (4). We then define the variance of $N_{i_c}(R)$,

$$\sigma^2(R) = \overline{N^2(R)} - \overline{N(R)}^2 \quad (15)$$

where $\overline{\dots}$ stands for the average over the center position i_c , as $\overline{\dots} := \frac{1}{N_{\text{site}}} \sum_{i_c} \dots$.

To characterize how the variance scales as a function of R , we employ two functions, namely, $A(R)$ and $\bar{B}(R)$. $A(R)$ is defined as

$$A(R) = \frac{\sigma^2(R)}{R}. \quad (16)$$

If this function becomes zero as R increases, it means that the variance grows slower than the volume of the region for which we define $N_{i_c}(R)$. In such a case, the distribution is called hyperuniform.

$\bar{B}(R)$ is defined as

$$\bar{B}(R) = \frac{1}{\bar{n}^2 R} \sum_{\mathcal{R}=0}^R \sigma^2(\mathcal{R}), \quad (17)$$

where \bar{n} is the average charge density. In the present case, we have $\bar{n} = \frac{1}{N_{\text{site}}} \sum_i n_i = \frac{1}{2}$. As is the case of the original definitions [36], we regard that the distribution belongs to the class-I hyperuniformity if $\bar{B}(R)$ converges to the constant value as R increases, and we call the value $\bar{B}(R \rightarrow \infty)$ the order metric. Note that the value of the order metric in

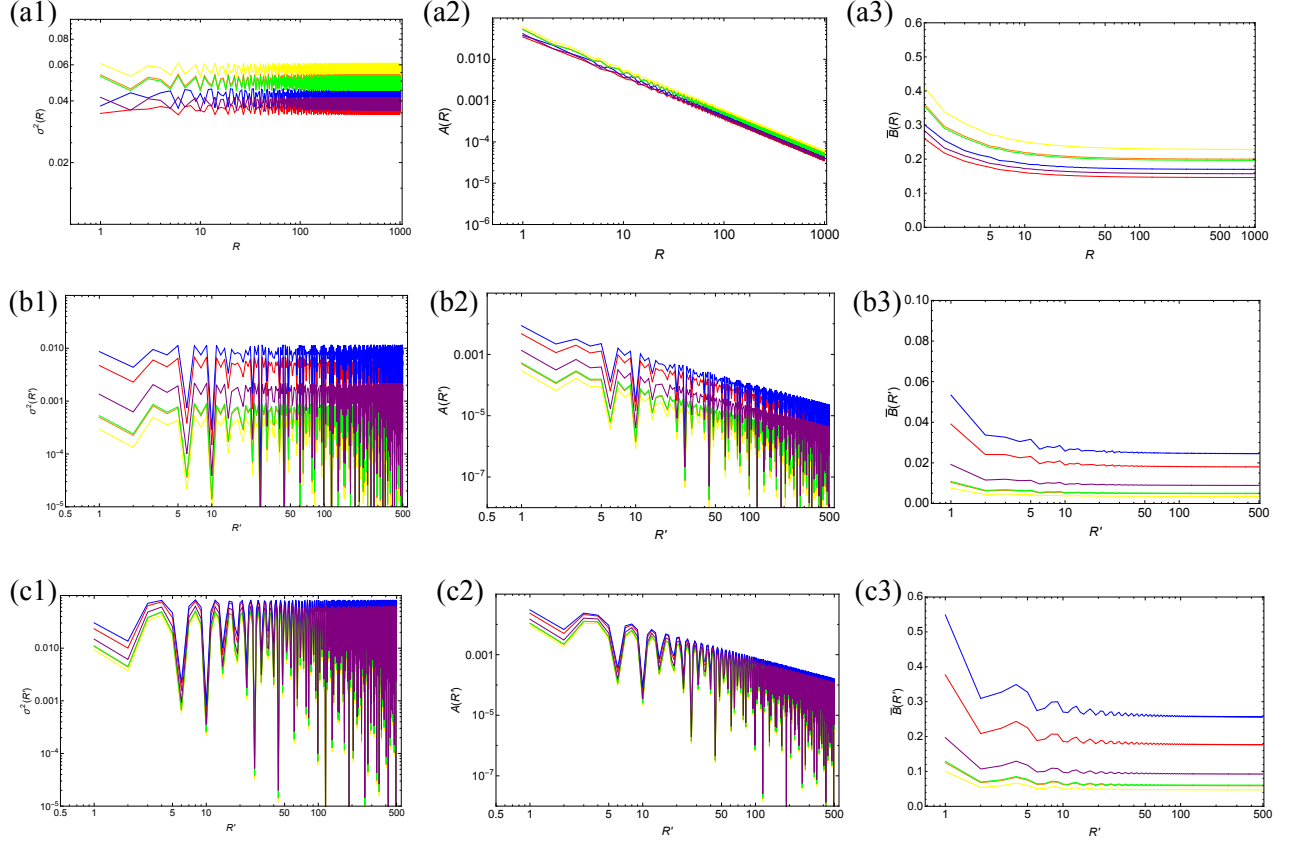


FIG. 7. The results for the hyperuniformity analysis for (a) the entire charge distribution, (b) the charge distribution for the A sublattice, and (c) the charge distribution for the B sublattice. The left, middle, and the right column represent σ^2 , A , and \bar{B} , respectively. The yellow, orange, green, purple, red, and blue lines are, respectively, the data for $\lambda = 0.5, 0.625, 0.645, 1, 2$, and 3 . Note that the distance R is measured with respect to the site index i , whereas R' is measured with respect to the unit cell index n .

this definition is not equal to that of the original definition, because we neglect the spatial fluctuation by the lattice-point configuration.

In Figs. 7(a1), 7(a2), and 7(a3), we plot the functions $\sigma^2(R)$, $A(R)$ and $\bar{B}(R)$, respectively. For $A(R)$, we see that $A(R)$ decreases as increasing R for all λ 's, revealing the hyperuniform nature of the charge distribution n_i . The qualitative nature of $\bar{B}(R)$ also does not depend on λ , and it goes to a constant value as increasing R , indicating that the distribution belongs to the class-I hyperuniformity. It is also to be noted that whether or not the histogram has a gap (Fig 5) does not affect the class of hyperuniformity, which is different from the original AAH model [39]. This may be due to the fact that the gap of the histogram in this model intrinsically arises from the existence of two distinct sublattices, unlike the AAH model. Quantitatively, the order metric behaves non-monotonically as a function of λ . Namely, for $\lambda < 2$, it decreases as increasing λ , and is minimized at $\lambda = 2$. Then, for $\lambda > 2$, the order metric increases again. This result provides another implication that $\lambda = 2$ is special.

We also perform the hyperuniformity analysis for the sublattice-resolved particle density distribution. In this case, the site label is equated with the unit-cell label n and the distance (represented by R') is measured in that unit. Also, \bar{n}

in Eq. (17) is replaced with $2\bar{n}^\alpha (= \frac{N_{\text{site}}}{L} \bar{n}^\alpha)$ ($\alpha = A, B$). We show the results in Figs. 7(b1)-(b3) for the A sublattice, and Figs. 7(c1)-(c3) for the B sublattice. We see that the particle density distributions for both sublattices again exhibit hyperuniformity of the class-I. Interestingly, the quantitative nature of the order metric is different from that in the total particle density distribution, in that, for both A and B sublattices, the order metric increases monotonically as increasing λ .

Before proceeding further, we note that, for any λ , the inversion participation ratio (IPR) defined for n_i scales as L^{-1} , which corresponds to the extended state. See Appendix B for details. This is a ubiquitous feature of the particle density distribution for the zero modes constructed from the MO representation [23–25].

IV. SINGLE-PARTICLE WAVE FUNCTIONS OF THE FINITE ENERGY MODES

So far, we have focused on the many-body state $|\Xi_0\rangle$. In this section, we argue the single-particle wave functions of the finite-energy modes. As we have mentioned, the energy spectrum of the finite-energy modes is identical to the AAH model up to the constant shift and the wave functions the

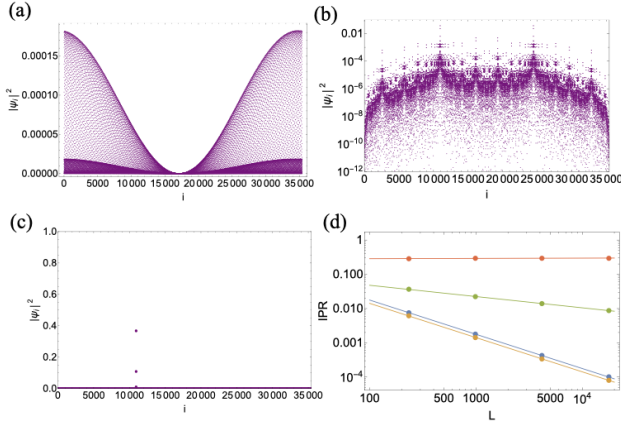


FIG. 8. Probability density for the lowest-finite-energy mode for (a) $\lambda = 0.5$, (b) $\lambda = 2$, and (c) $\lambda = 3$. (d) IPR for the lowest finite-energy mode [Eq. (18)]. Blue, orange, green, and red dots are for $\lambda = 0.5, 1, 2$, and 3 , respectively, and the lines are the fitting curve $\text{IPR} = x \cdot L^{-y}$.

finite-energy modes are also related to those of \mathcal{O} . Hence, for the finite-energy modes, it is expected that the transition from extended state to the localized state occurs upon increasing λ [47].

In Figs. 8(a)-(c), we plot the real-space probability density profile for the lowest energy mode. It shows the extended profile for $\lambda = 0.5$, while it shows the localized profile for $\lambda = 3$. For $\lambda = 2$, a rather complex behavior appears, which indicates its critical nature. We further investigate the scaling behavior of the finite-energy eigenmodes to see whether the properties of the AAH model are indeed inherited or not. To this end, we compute the IPR for the finite-energy mode which is defined as

$$\text{IPR} = \sum_i |\psi_{\ell,i}|^4, \quad (18)$$

where $\psi_{\ell,i}$ stands for the normalized wave function of the ℓ th finite-energy mode. The IPR scales against the system size as $\text{IPR} \propto L^{-d}$ (with d being the spatial dimension) for extended states, whereas it scales as $\text{IPR} \propto (\text{const.})$ for the localized states. In Fig. 8(d), we plot the IPR for the lowest finite energy mode for $\lambda = 0.5, 1, 2$, and 3 . Here we use the data for $L = 233, 987, 4181$, and 17711 . We fit the IPR as $\text{IPR} = x \cdot L^{-y}$. We find that $y \sim 1$ for $\lambda = 0.5$ and 1 , and $y \sim 0$ for $\lambda = 3$. At $\lambda = 2$, the IPR shows the intermediate scaling, $y \sim 0.33$, indicating the critical behavior of the wave function. From these results, we conclude that the extended-to-localization transition of the finite-energy modes coincides with that of the original AAH model.

V. SUMMARY

We have proposed a quasi-periodic flat-band model, that has macroscopically-degenerate zero-energy modes, and whose finite-energy modes have the same eigenvalues as that of the AAH model. We have found that the many-body state

with the zero-energy modes being fully occupied has a characteristic particle density distribution, namely, it belongs to the class-I hyperuniformity regardless of the parameter λ . The parameter $\lambda = 2$, which is the critical point of the original AAH model, is special in that the particle densities of two sublattices balance, and the order metric for the particle density distribution is minimized. As for the finite-energy modes, we find that the extended-to-localized transition coincides with that of the original AAH model. This results from the fact that the finite energy modes are given by the products of Ψ and the eigenmodes of the AAH model.

We close this paper by addressing several extensibilities of our model construction. First, it can be generalized to the series of one-dimensional lattices where a unit cell contains $M - 1$ sublattices and the MO is expressed as a linear combination of M MOs. See Appendix C for details. Second, by changing the coefficients of $d_{n,B}$ in Eq. (1), we can make counterparts of tight-binding chains with the uniform-strength hopping integrals and the spatially dependent on-site potential. Hence, we can make the counterpart of the quasi-periodic models of this kind, for example, the diagonal Fibonacci chain [48, 49] and an exactly solvable quasi-periodic chain due to quantum group structure [50, 51]. Case studies of various models will be an interesting future problem.

ACKNOWLEDGMENTS

The authors thank Shiro Sakai and Takumi Kuroda for fruitful discussions. This work is supported by JSPS, KAKENHI, Grant No. JP23K03243 (TM) and No. JP23K25788 (YH).

Appendix A: Sublattice-dependence of filling fraction at $\lambda = 2$

Here we prove that $\bar{n}^A = \bar{n}^B = \frac{1}{4}$ for $\lambda = 2$ (Fig. 6). As is the case with the main text, we set $\phi = \phi' = 0$ in the following.

As we have mentioned in the main text, \mathcal{O} corresponds to the Hamiltonian matrix of the AAH model with the constant energy shift. To make this fact manifest, we write $\mathcal{O} = \mathcal{H}^{\text{AAH}} + (2 + \lambda)\mathcal{I}_L$, where \mathcal{H}^{AAH} is the Hamiltonian matrix of the AAH model and \mathcal{I}_L is the $L \times L$ identity matrix. Due to this, the eigenenergy of ε_ℓ can be written as $\varepsilon_\ell = \varepsilon_\ell^{\text{AAH}} + (2 + \lambda)$. We further divide \mathcal{H}^{AAH} into two parts, $\mathcal{H}^{\text{AAH}} = \mathcal{H}^{\text{kin}} + \mathcal{H}^{\text{pot}}$, where $[\mathcal{H}^{\text{kin}}]_{n,n'} = \delta_{n,n'+1} + \delta_{n,n'-1}$ denotes the kinetic energy part and $[\mathcal{H}^{\text{pot}}]_{n,n'} = \lambda \cos\left(\frac{2\pi n}{\tau}\right) \delta_{n,n'}$ denotes the potential energy part. For future use, we also rewrite the inverse matrix of \mathcal{O} by using its eigenvectors, as

$$[\mathcal{O}^{-1}]_{n,n'} = \sum_\ell \frac{[\varphi_\ell]_n [\varphi_\ell]_{n'}^*}{\varepsilon_\ell}. \quad (A1)$$

Now we calculate $\bar{n}^{A/B}$ from Eq. (12). Using Eq. (6), we

have

$$\begin{aligned}
 \bar{n}^A &= \frac{1}{N_{\text{site}}} \sum_n \left[1 - (\Psi \mathcal{O}^{-1} \Psi^\dagger)_{(n,A),(n,A)} \right] \\
 &= \frac{1}{2} - \frac{1}{2L} \sum_{n,n',n'',\ell} \frac{[\Psi]_{(n,A),n'} [\varphi_\ell]_{n'} [\varphi_\ell]_{n''}^* [\Psi^\dagger]_{n'',(n,A)}}{\varepsilon_\ell} \\
 &= \frac{1}{2} - \frac{1}{2L} \sum_{n,\ell} \frac{2[\varphi_\ell]_n [\varphi_\ell]_n^* + [\varphi_\ell]_n ([\varphi_\ell]_{n-1}^* + [\varphi_\ell]_{n+1}^*)}{\varepsilon_\ell}.
 \end{aligned} \tag{A2}$$

To proceed, we point out that $\sum_n [\varphi_\ell]_n [\varphi_\ell]_n^* = 1$ and $\sum_n [\varphi_\ell]_n ([\varphi_\ell]_{n-1}^* + [\varphi_\ell]_{n+1}^*) = \langle \mathcal{H}^{\text{kin}} \rangle_\ell$, where $\langle \mathcal{A} \rangle_\ell$ represents the expectation value of \mathcal{A} with respect to φ_ℓ . Substituting these into Eq. (A2), we have

$$\bar{n}^A = \frac{1}{2} - \frac{1}{2L} \sum_\ell \frac{2 + \langle \mathcal{H}^{\text{kin}} \rangle_\ell}{\varepsilon_\ell}. \tag{A3}$$

Similarly, for \bar{n}^B , we have

$$\begin{aligned}
 \bar{n}^B &= \frac{1}{N_{\text{site}}} \sum_n \left[1 - (\Psi \mathcal{O}^{-1} \Psi^\dagger)_{(n,B),(n,B)} \right] \\
 &= \frac{1}{2} - \frac{1}{2L} \sum_{n,n',n'',\ell} \frac{[\Psi]_{(n,B),n'} [\varphi_\ell]_{n'} [\varphi_\ell]_{n''}^* [\Psi^\dagger]_{n'',(n,B)}}{\varepsilon_\ell} \\
 &= \frac{1}{2} - \frac{1}{2L} \sum_{n,\ell} \frac{2\lambda \cos^2\left(\frac{\pi}{\tau} n\right) [\varphi_\ell]_n [\varphi_\ell]_n^*}{\varepsilon_\ell} \\
 &= \frac{1}{2} - \frac{1}{2L} \sum_{n,\ell} \frac{\lambda [1 + \cos\left(\frac{2\pi}{\tau} n\right)] [\varphi_\ell]_n [\varphi_\ell]_n^*}{\varepsilon_\ell} \\
 &= \frac{1}{2} - \frac{1}{2L} \sum_\ell \frac{\lambda + \langle \mathcal{H}^{\text{pot}} \rangle_\ell}{\varepsilon_\ell}.
 \end{aligned} \tag{A4}$$

We now focus on the case of $\lambda = 2$, which is the self-dual point of the AAH model. Actually, at this point, the kinetic energy and the potential energy are equal to each other, namely, $\langle \mathcal{H}^{\text{kin}} \rangle_\ell = \langle \mathcal{H}^{\text{pot}} \rangle_\ell = \frac{\varepsilon_\ell^{\text{AAH}}}{2}$ for all ℓ due to the duality [31, 52]. Substituting this into Eqs. (A3) and (A4), as well as $\lambda = 2$, we have

$$\bar{n}^A = \frac{1}{2} - \frac{1}{2L} \sum_\ell \frac{2 + \frac{\varepsilon_\ell^{\text{AAH}}}{2}}{4 + \varepsilon_\ell^{\text{AAH}}} = \frac{1}{4}, \tag{A5}$$

and

$$\bar{n}^B = \frac{1}{2} - \frac{1}{2L} \sum_\ell \frac{2 + \frac{\varepsilon_\ell^{\text{AAH}}}{2}}{4 + \varepsilon_\ell^{\text{AAH}}} = \frac{1}{4}. \tag{A6}$$

Appendix B: IPR for zero-energy modes

In this appendix, we address the scaling of the IPR for n_i . The IPR for the degenerate zero-energy modes is defined as

$$\text{IPR}^{(\text{ZM})} = \sum_i \left(\frac{n_i}{L} \right)^2. \tag{B1}$$

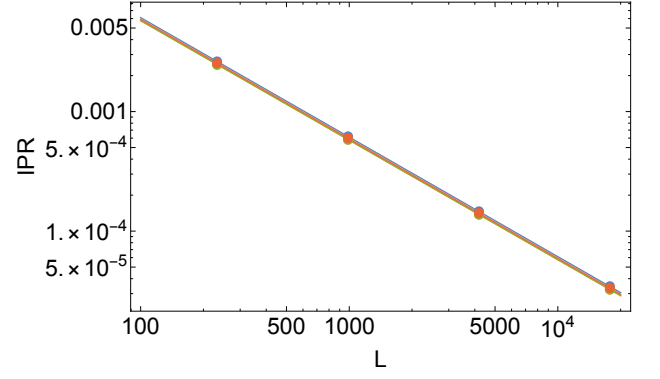


FIG. 9. IPR for the degenerate zero modes [Eq. (B1)]. Blue, orange, green, and red dots are for $\lambda = 0.5, 1, 2$, and 3 , respectively, and the lines are the fitting curve $\text{IPR} = x \cdot L^{-y}$.

In Fig. 9, we plot the size dependence of $\text{IPR}^{(\text{ZM})}$ for several values of λ . We see that the $\text{IPR}^{(\text{ZM})}$ has very small λ dependence. In fact, for all values of λ , $\text{IPR}^{(\text{ZM})}$ scales as $\text{IPR}^{(\text{ZM})} \propto L^{-1}$, which is the same behavior as the extended states. Notably, this behavior is in common with the random MO models [23–25], hence we expect that this behavior is ubiquitous for the degenerate zero-energy modes for the MO models.

Appendix C: Extension of the model construction scheme

In the saw-tooth lattice model, a unit cell contains two sublattices and the MO is expressed as a linear combination of three AOs. In this appendix, we show a generalization where a unit cell contains $M - 1$ sublattices and the MO is expressed as a linear combination of M MOs.

For concreteness, let us focus on the case of $M = 4$. We consider the Hamiltonian on the diamond chain [Fig. 10(a)]. The Hamiltonian is again written in the form $H = \sum_n D_n^\dagger D_n$ with

$$\begin{aligned}
 D_n &= e^{-i\phi'/2} d_{n,A} + \sqrt{\lambda} \cos\left(\frac{\pi}{\tau} n + \frac{\phi}{2}\right) d_{n,B} \\
 &\quad + \sqrt{\lambda} \cos\left(\frac{\pi}{\tau} n + \frac{\phi}{2}\right) d_{n,C} + e^{i\phi'/2} d_{n+1,A}
 \end{aligned} \tag{C1}$$

See Fig. 10(b) for the schematic figure of the MO in Eq. (C1). In this model, there are $3L$ AOs and L MOs, hence the degeneracy of the zero-energy modes is $2L$. Notice that the corresponding \mathcal{O} for the present model is exactly the same as that for the saw-tooth lattice model. Hence, the energy eigenvalues

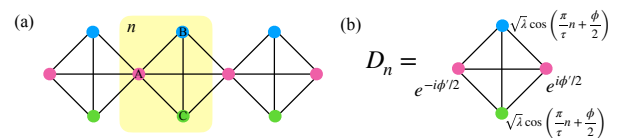


FIG. 10. (a) Schematic figures of the diamond chain model and (b) the MO of Eq. (C1).

of the finite-energy modes are again the same as those for the AAH model.

In Figs. 11(a)-11(d), we plot the particle density distribution for the many-body state with the degeneracy of the zero-energy modes being fully occupied. Note that the filling factor of this many-body state is $2/3$. We see that the qualitative feature is the same as that for the saw-tooth lattice model, in that the A sublattice has smaller fluctuations than those of the B and C sublattice.

Figure 11(e) shows the sublattice-resolved filling fraction as a function of λ . We see that the particle density of the sublattice A becomes larger as we increase λ . Interestingly, at $\lambda = 2$, we have a characteristic rational filling fraction, $\bar{n}^A = \frac{1}{6}$ and $\bar{n}^B = \bar{n}^C = \frac{1}{4}$.

The extension of the present model whose MO is composed of the M -site cluster is straightforward. In such models, the degeneracy of the zero-energy modes is $(M - 2)L$, hence the filling factor of the many-body state with the zero-energy modes being fully occupied is $(M - 2)/(M - 1)$. We have numerically confirmed that, at $\lambda = 2$, each sublattice has a characteristic rational filling fraction: $\bar{n}^A = \frac{1}{2(M-1)}$ and $\bar{n}^{\eta \neq A} = \frac{2M-5}{2(M-1)(M-2)}$, where we refer to the sublattice being shared with different clusters as A.

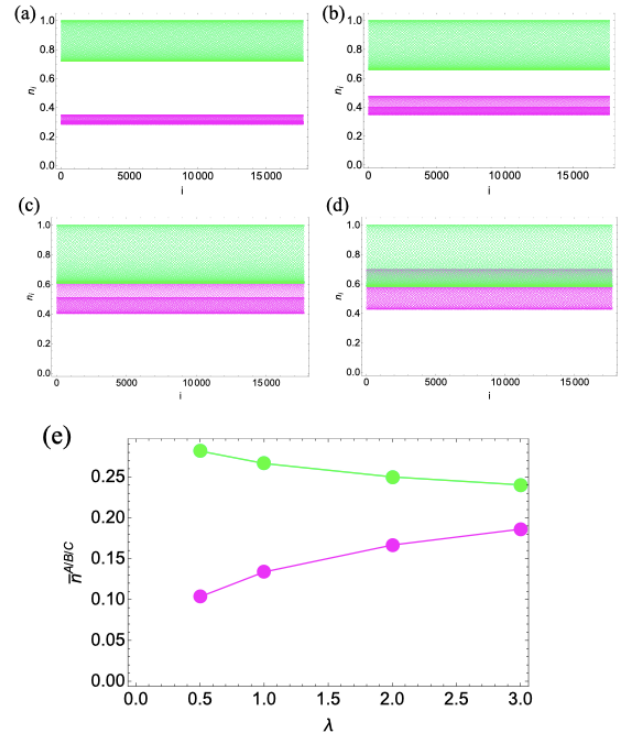


FIG. 11. The real space particle density distribution for the diamond chain model. The parameters are $\phi = \phi' = 0$ and (a) $\lambda = 0.5$, (b) $\lambda = 1$, (c) $\lambda = 2$, and (d) $\lambda = 3$. The magenta, cyan, and green points are the data for the sublattices A, B, and C, respectively. Note that the cyan points are unseen because they overlap with the green points. (e) Sublattice-resolved filling fraction as a function of λ . Magenta, cyan, and green points represent the A, B, and C sublattices, respectively.

-
- [1] B. Sutherland, Localization of electronic wave functions due to local topology, *Phys. Rev. B* **34**, 5208 (1986).
 - [2] A. Mielke, Ferromagnetism in the Hubbard model on line graphs and further considerations, *Journal of Physics A: Mathematical and General* **24**, 3311 (1991).
 - [3] H. Tasaki, Ferromagnetism in the Hubbard models with degenerate single-electron ground states, *Phys. Rev. Lett.* **69**, 1608 (1992).
 - [4] J. Schulenburg, A. Honecker, J. Schnack, J. Richter, and H.-J. Schmidt, Macroscopic Magnetization Jumps due to Independent Magnons in Frustrated Quantum Spin Lattices, *Phys. Rev. Lett.* **88**, 167207 (2002).
 - [5] M. E. Zhitomirsky and H. Tsunetsugu, Exact low-temperature behavior of a kagomé antiferromagnet at high fields, *Phys. Rev. B* **70**, 100403 (2004).
 - [6] D. L. Bergman, C. Wu, and L. Balents, Band touching from real-space topology in frustrated hopping models, *Phys. Rev. B* **78**, 125104 (2008).
 - [7] D. Leykam, A. Andreanov, and S. Flach, Artificial flat band systems: from lattice models to experiments, *Advances in Physics: X* **3**, 1473052 (2018).
 - [8] T. Mizoguchi, Y. Kuno, and Y. Hatsugai, Flat band, spin-1 Dirac cone, and Hofstadter diagram in the fermionic square kagome model, *Phys. Rev. B* **104**, 035161 (2021).
 - [9] M. Goda, S. Nishino, and H. Matsuda, Inverse Anderson Transition Caused by Flatbands, *Phys. Rev. Lett.* **96**, 126401 (2006).
 - [10] S. Nishino, H. Matsuda, and M. Goda, Flat-Band Localization in Weakly Disordered System, *J. Phys. Soc. Jpn.* **76**, 024709 (2007).
 - [11] J. T. Chalker, T. S. Pickles, and P. Shukla, Anderson localization in tight-binding models with flat bands, *Phys. Rev. B* **82**, 104209 (2010).
 - [12] D. Leykam, J. D. Bodyfelt, A. S. Desyatnikov, and S. Flach, Localization of weakly disordered flat band states, *The European Physical Journal B* **90**, 1 (2017).
 - [13] A. Ramachandran, A. Andreanov, and S. Flach, Chiral flat bands: Existence, engineering, and stability, *Phys. Rev. B* **96**, 161104 (2017).
 - [14] P. Shukla, Disorder perturbed flat bands: Level density and inverse participation ratio, *Phys. Rev. B* **98**, 054206 (2018).
 - [15] P. Shukla, Disorder perturbed flat bands. II. Search for criticality, *Phys. Rev. B* **98**, 184202 (2018).
 - [16] T. Bilitewski and R. Moessner, Disordered flat bands on the kagome lattice, *Phys. Rev. B* **98**, 235109 (2018).
 - [17] A. Nandy, Tunable caging of excitation in decorated Lieb-ladder geometry with long-range connectivity, *Chinese Physics B* **32**, 127201 (2023).
 - [18] Y. Kim, T. Čadež, A. Andreanov, and S. Flach, Flat band in-

- duced metal-insulator transitions for weak magnetic flux and spin-orbit disorder, *Phys. Rev. B* **107**, 174202 (2023).
- [19] A. Mallick, N. Chang, W. Maimaiti, S. Flach, and A. Andreanov, Wannier-Stark flatbands in Bravais lattices, *Phys. Rev. Res.* **3**, 013174 (2021).
- [20] T. Mizoguchi, Y. Kuno, and Y. Hatsugai, Blocking particle dynamics in a diamond chain with spatially increasing flux, *Phys. Rev. A* **109**, 053315 (2024).
- [21] S. Lee, S. Flach, and A. Andreanov, Critical state generators from perturbed flatbands, *Chaos: An Interdisciplinary Journal of Nonlinear Science* **33**, 073125 (2023).
- [22] Y.-C. Zhang, Critical regions in a one-dimensional flat band lattice with a quasi-periodic potential, *Scientific Reports* **14**, 17921 (2024).
- [23] Y. Hatsugai, Revisiting Flat bands and localization, *Annals of Physics* **435**, 168453 (2021), special Issue on Localisation 2020.
- [24] T. Kuroda, T. Mizoguchi, H. Araki, and Y. Hatsugai, Machine Learning Study on the Flat-Band States Constructed by Molecular-Orbital Representation with Randomness, *Journal of the Physical Society of Japan* **91**, 044703 (2022).
- [25] T. Mizoguchi and Y. Hatsugai, Molecular-orbital representation with random $U(1)$ variables, *Phys. Rev. B* **107**, 094201 (2023).
- [26] Y. Hatsugai and I. Maruyama, Z_Q topological invariants for Polyacetylene, Kagome and Pyrochlore lattices, *EPL (Europhysics Letters)* **95**, 20003 (2011).
- [27] Y. Hatsugai, K. Shiraishi, and H. Aoki, Flat bands in the Weaire–Thorpe model and silicene, *New Journal of Physics* **17**, 025009 (2015).
- [28] T. Mizoguchi and Y. Hatsugai, Molecular-orbital representation of generic flat-band models, *EPL (Europhysics Letters)* **127**, 47001 (2019).
- [29] T. Mizoguchi and Y. Hatsugai, Systematic construction of topological flat-band models by molecular-orbital representation, *Phys. Rev. B* **101**, 235125 (2020).
- [30] T. Mizoguchi and Y. Hatsugai, Hidden chiral symmetry for the kagome lattice and its analogs, *Phys. Rev. B* **111**, 085150 (2025).
- [31] S. Aubry and G. André, Analyticity breaking and Anderson localization in incommensurate lattices, Proceedings, VIII International Colloquium on Group-Theoretical Methods in Physics **3** (1980).
- [32] P. G. Harper, Single Band Motion of Conduction Electrons in a Uniform Magnetic Field, *Proceedings of the Physical Society. Section A* **68**, 874 (1955).
- [33] S. Torquato and F. H. Stillinger, Local density fluctuations, hyperuniformity, and order metrics, *Phys. Rev. E* **68**, 041113 (2003).
- [34] C. E. Zachary and S. Torquato, Hyperuniformity in point patterns and two-phase random heterogeneous media, *Journal of Statistical Mechanics: Theory and Experiment* **2009**, P12015 (2009).
- [35] E. C. Oğuz, J. E. S. Socolar, P. J. Steinhardt, and S. Torquato, Hyperuniformity of quasicrystals, *Phys. Rev. B* **95**, 054119 (2017).
- [36] S. Torquato, Hyperuniform states of matter, *Physics Reports* **745**, 1 (2018).
- [37] E. Chertkov, R. A. DiStasio, G. Zhang, R. Car, and S. Torquato, Inverse design of disordered stealthy hyperuniform spin chains, *Phys. Rev. B* **93**, 064201 (2016).
- [38] S. Sakai, R. Arita, and T. Ohtsuki, Hyperuniform electron distributions controlled by electron interactions in quasicrystals, *Phys. Rev. B* **105**, 054202 (2022).
- [39] S. Sakai, R. Arita, and T. Ohtsuki, Quantum phase transition between hyperuniform density distributions, *Phys. Rev. Res.* **4**, 033241 (2022).
- [40] S. Sakai, Hyperuniform electron distributions on the ammann-beenker tiling, *Journal of Physics: Conference Series* **2461**, 012002 (2023).
- [41] M. Hori, T. Sugimoto, Y. Hashizume, and T. Tohyama, Multifractality and Hyperuniformity in Quasicrystalline Bose–Hubbard Models with and without Disorder, *Journal of the Physical Society of Japan* **93**, 114005 (2024).
- [42] D. Chen, R. Samajdar, Y. Jiao, and S. Torquato, Anomalous suppression of large-scale density fluctuations in classical and quantum spin liquids, *Proceedings of the National Academy of Sciences* **122**, e2416111122 (2025).
- [43] T. Mizoguchi, Y. Kuno, and Y. Hatsugai, Construction of interacting flat-band models by molecular-orbital representation: Correlation functions, energy gap, and entanglement, *Progress of Theoretical and Experimental Physics* **2022**, 023102 (2022).
- [44] To be precise, we define the Fibonacci sequence as $F_1 = 1$, $F_2 = 1$, $F_n = F_{n-1} + F_{n-2}$ ($n \geq 3$).
- [45] A. Koga and S. Sakai, Hyperuniformity in two-dimensional periodic and quasiperiodic point patterns, *Phys. Rev. E* **109**, 044103 (2024).
- [46] A. Koga, S. Sakai, Y. Matsushita, and T. Ishimasa, Hyperuniform properties of square-triangle tilings, *Phys. Rev. B* **110**, 094208 (2024).
- [47] M. Kohmoto, Metal-Insulator Transition and Scaling for Incommensurate Systems, *Phys. Rev. Lett.* **51**, 1198 (1983).
- [48] M. Kohmoto, L. P. Kadanoff, and C. Tang, Localization Problem in One Dimension: Mapping and Escape, *Phys. Rev. Lett.* **50**, 1870 (1983).
- [49] S. Ostlund, R. Pandit, D. Rand, H. J. Schellnhuber, and E. D. Siggia, One-Dimensional Schrödinger Equation with an Almost Periodic Potential, *Phys. Rev. Lett.* **50**, 1873 (1983).
- [50] Y. Hatsugai, M. Kohmoto, and Y.-S. Wu, Explicit Solutions of the Bethe Ansatz Equations for Bloch Electrons in a Magnetic Field, *Phys. Rev. Lett.* **73**, 1134 (1994).
- [51] Y. Hatsugai, M. Kohmoto, and Y.-S. Wu, Quantum group, Bethe ansatz equations, and Bloch wave functions in magnetic fields, *Phys. Rev. B* **53**, 9697 (1996).
- [52] M. Kohmoto, Zero modes and the quantized Hall conductance of the two-dimensional lattice in a magnetic field, *Phys. Rev. B* **39**, 11943 (1989).